crystals

MDPI

Article

The Surface-Roughness Effects on Light Beam Interactions between the CsI Phosphor and Optical Sensing Materials

Panagiotis Liaparinos [1,*] and Stratos David [1,2]

[1] Radiation Physics, Materials Technology and Biomedical Imaging Laboratory, Department of Biomedical Engineering, University of West Attica, 12210 Athens, Greece; sdavid@uniwa.gr
[2] Department of Medical Physics, University of Patras, 26504 Rion, Greece
* Correspondence: liapkin@uniwa.gr

Received: 11 February 2020; Accepted: 4 March 2020; Published: 5 March 2020

Abstract: In digital phosphor-based imaging modalities, one important intermediate stage is the optical coupling between the phosphor material and the optical sensor. The performance of the optical compatibility is affected by surface-roughness issues, for which further research should be paid. This paper investigates the surface-roughness influence between the CsI phosphor material and the optical sensing materials (i.e., the silicon dioxide—SiO_2, the indium tin oxide—ITO, and the indium gallium arsenide—InGaAs) employed in several image devices. Results showed that for all sensing materials, the transmission factor t of the optical signal follows qualitatively the variation of their refractive indexes and quantitatively the variation of the surface roughness and the incident polar angle. Finally, with respect to light wavelength, the curve of variation was found to be continuous for ITO and SiO_2 sensing materials; however, lower and sharper variations were observed in the first case.

Keywords: surface roughness; light interactions; phosphor materials; optical sensors

1. Introduction

Optical sensors are devices, usually incorporating a sensing material, which convert the light quanta into electronic signals. They are often used to measure physical quantities (e.g., pressure, flow, temperature) of an instrument by detecting and translating the characteristics of light (e.g., frequency, wavelength, polarization), or by performing measurements of light variations (e.g., intensity, distribution). Optical sensors are used in numerous applications, either for research or commercial purposes, and their technology has found significant implementations in various scientific fields such as: environmental monitoring, metrology, particle counting and characterization, pharmaceuticals, biotechnology, etc.

In the field of biomedical imaging, the optical sensor is considered as a required and significant tool in the imaging chain, which is generally located at the position of the system where the final image is formed. In particular, in indirect digital medical systems, the optical sensor is part of the phosphor-based radiation detector, which consists of a serial chain of signal components, such as phosphors, fiber optics or lenses, image intensifiers and the sensor pixel array. The phosphor, either the CsI columnar structure or the Gd_2O_2S powder synthesis [1], converts the ionizing radiation (e.g., the X-rays) into optical signals, a sensing material (e.g., a photodiode) detects and transforms the optical signals to electron carries, and finally a readout pixel array system produces the gray-scale image with respect to the integration of the electron flow intensity. Today, several devices have been developed that implement various types of digital optical sensors, including: (a) commercial systems, such as: (i) charge-coupled devices (CCD) devices, (ii) thin-film transistor (TFT) devices, (iii) complementary

metal-oxide-semiconductor (CMOS) devices [2–5], and (b) forward-looking systems, such as: (i) digital integration sensors (DIS), and (ii) quantum image sensors (QIS) [6]. The advantages, disadvantages, limitations, and further challenges of each image sensor have extensively been analyzed [2–6].

In most, if not all, cases, different detector technologies necessitate compromises among the following factors: field coverage, geometrical characteristics, quantum efficiency, sensitivity, dynamic range, uniformity, acquisition speed, the power consumption and supply, electronic read out mechanisms, frame rate, and cost [2,3]. Based on the necessities of the imaging task, crucial factors in the digitization process can also be considered to be the pixel size and the bit depth, which affect the spatial resolution and noise characteristics. However, since the image quality is related to light characteristics, a lot of attention has been focused on either phosphor improvement (i.e., the synthesis of new materials of optimized chemical [7,8], optical [9–11], and structural properties [11–13] or advanced optical sensor development. Particular research has also been carried out on the optical compatibility [14] (i.e., the optical matching) between the phosphor material and the optical sensor. Although several studies have been performed for a variety of issues, as described above, further investigation discussing the effects of the roughness of surface between the phosphor material and the sensing material of the optical sensor is required. In general, different modeling approaches have been employed for the determination of surface-roughness effects on: (i) light scattering modeling [15], (ii) optical properties and sensitivity [16], (iii) reflectance [17], (iv) transmission capacities of optical fibers [18], and (v) the overall performance of a sensor [19]. On the other hand, several instrumentation technologies (laser-based [20,21], LED-based [22], or reflective [23] fiber-optic sensors) and different methodologies [24,25] have been developed to measure, assess, and finally characterize the properties of surface roughness.

The aim of this manuscript is to use a simple model and provide a wider understanding of roughness effects on optical coupling especially observed in phosphor-based imaging systems. The present examination considered the coupling of CsI phosphor with three cases of sensing materials: (i) silicon dioxide (SiO_2) material employed in charge-coupled devices (CCD), (ii) indium tin oxide (ITO) material used in thin-film transistor (TFT) devices, and (iii) indium gallium arsenide (InGaAs) applied in complementary metal-oxide-semiconductor (CMOS) devices.

2. Materials and Methods

2.1. Evaluation of Diffuse Intensity Reflectance and Transmittance

In digital imaging systems, during the light detection process, light photons are emitted from the phosphor material and thereafter are recorded by the optical detector. However, during this procedure, when light photons hit one of the phosphor layer boundaries, they may either pass to the optical sensor or internally be reflected.

2.2. The Case of Surface Smoothness

In the case of surface smoothness (the interface between the phosphor and the optical sensor is smooth as shown in Figure 1a), the angle of transmission ω is calculated as a function of the angle of incidence θ with the help of Snell's law according to the following formula:

$$\theta = \cos^{-1}(|\cos\theta|) \text{ and } \omega = \sin^{-1}\left(\frac{n_{origin}}{n_{receiving}}\sin\theta\right) \quad (1)$$

where n_{origin} is the refractive index of the origin medium (the phosphor layer) and $n_{receiving}$ is the refractive index of the receiving medium (the optical sensor). Using Fresnel's formulas, the probability of the optical reflectance *Rs* and transmittance *Ts* is evaluated as follows [26–28]:

$$Rs = \frac{1}{2}\left(\frac{\sin^2(\theta-\omega)}{\sin^2(\theta+\omega)} + \frac{\tan^2(\theta-\omega)}{\tan^2(\theta+\omega)}\right) \text{ and } Ts = 1 - R \quad (2)$$

taking into account the average of the reflectances for the two orthogonal polarization directions [29]:

$$R\,II = \frac{\tan^2(\theta-\omega)}{\tan^2(\theta+\omega)} \text{ and } R\perp = \frac{\sin^2(\theta-\omega)}{\sin^2(\theta+\omega)} \tag{3}$$

2.3. The Effect of Surface Roughness

In the case of surface roughness (the interface between the phosphor and the optical sensor is rough as shown in Figure 1b), the Fresnel's formulas are modified by taking into account a factor that depends on the granularity of the interface and the evaluation of reflectance *Rr* and transmittance *Tr* is given below [30–33]:

$$r = 1 - \exp\left[-\left(\frac{4\pi n_{origin}\quad \delta}{\lambda}\cos\theta\right)^2\right] \text{ and } Rr = r \quad Rs \tag{4}$$

and

$$t = 1 - \exp\left[-\left(\frac{4\pi\left(\quad n_{origin} - n_{receiving}\right)\quad \delta}{\lambda}\cos\theta\right)^2\right] \tag{5}$$

where δ is the surface roughness expressing the area of surface irregularities profile per unit of length, λ is the light wavelength, n_{origin} is the refractive index of the medium of origin, $n_{receiving}$ is the refractive index of the receiving medium, and θ is the incident angle. Values of r and t near to unity imply reflectance and transmittance similar to those of surface smoothness. It is of significance to note that equations (4) and (5) have suitably been modified so as to provide results for particular angles.

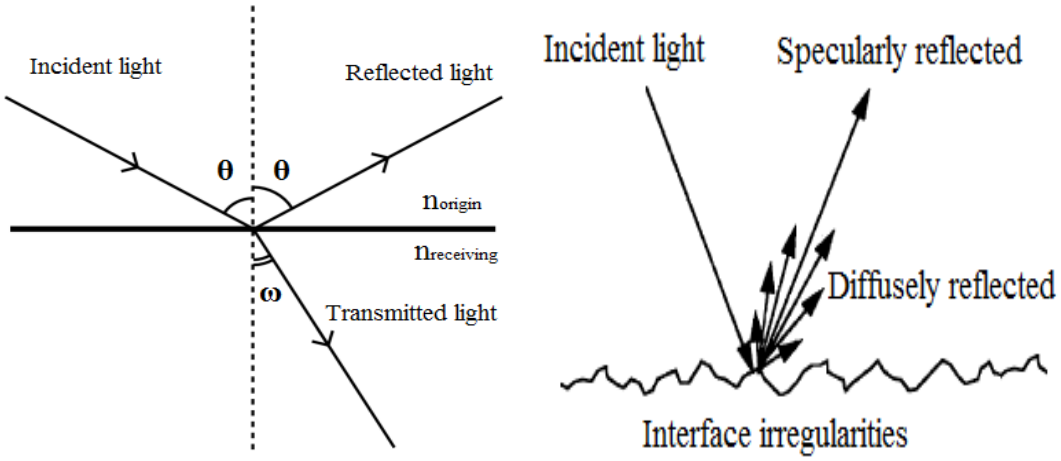

(**a**) Smoothness surface (**b**) Roughness effect

Figure 1. The figure illustrates the light ray interaction with the surface (the interface between the phosphor and the optical sensor) in case of: (**a**) smooth surface and (**b**) rough surface.

2.4. Set Up of Phosphor–Optical Detector Combinations

In the present study, the surface-roughness effects between the phosphor and optical sensor were evaluated for the most widely used phosphor material in indirect phosphor-based medical imaging detectors, which is the CsI phosphor (i.e., the geometry of the detector consists of CsI phosphor coupled with the sensing layer of the optical sensor, as illustrated in Figure 2).

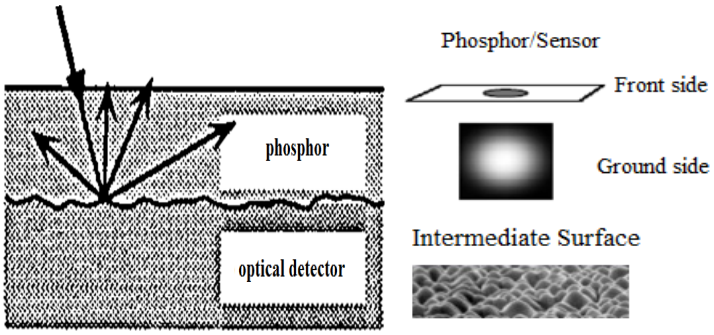

Figure 2. The figure illustrates the geometry of the present study (the configuration between the phosphor and the optical sensor).

Its columnar (needle-like) structure is employed in imaging systems to improve the X-ray quanta detection while controlling lateral dispersion of the signal due to optical transport [29]. In addition, this property allows the CsI layer to be made thicker than other phosphor layers (i.e., for the same amount of spatial spread of the signal), the increased thickness allows higher X-ray absorption and as a result CsI generally produces equivalent image quality at lower X-ray exposure levels than Gd_2O_2S-based detectors [1].

Thus, the CsI phosphor provides excellent resolution, through reduced scattering, since each column acts as a light pipe channeling the visible light to the optical sensor. The aforementioned conditions make the CsI phosphor prevalent and provide an advantage over the traditional, popular and cost-effective gadolinium oxysulfide (Gd_2O_2S) granular phosphor, although its technology is well-known, and its size, thickness, and flexibility can be handled easily [34]. Due to the slightly hydroscopic nature, columnar crystalline structures are obtained via a deposition process on specially treated substrates, and coatings are often encapsulated against moisture ingress, which also eliminate damage from transit and handling. Last but not least, the CsI phosphor can be readily deposited by thermal evaporation onto a readout pixel array without degrading the properties of active devices in the array. This direct deposition avoids the use of the optical coupling agents, such as optical grease or coupling fluid, between the scintillator and the readout pixel array [34]. The value of CsI refractive index is often given stable (value equal to 1.8) in literature; however, in the present study, it was considered to vary with light wavelength, as shown in Figure 3 [35].

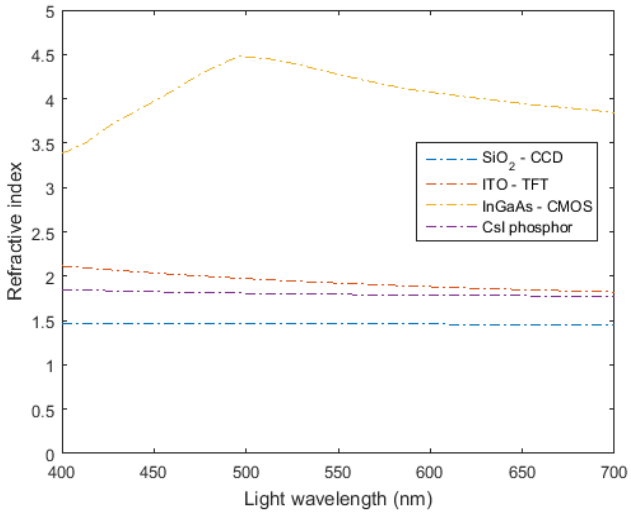

Figure 3. The refractive index as a function of light wavelength (400–700 nm). Figure depicts the refractive index of CsI phosphor and the corresponding refractive indices of three sensing materials: (1) SiO_2 (employed in charge-coupled devices (CCD)), (2) ITO (employed in thin-film transistor (TFT) devices) and (3) InGaAs (employed in complementary metal-oxide-semiconductor (CMOS) devices).

Below the phosphor material, the compatibility with the optical sensors is mainly served by a photodiode. This device is capable of converting light into electric current and thus being able to sense light intensity (i.e., as light hits the photodiode, free electrons will be generated and the current flowing in the circuit will increase) [36]. Three cases of sensing materials were assumed as the intermediate stage between the phosphor and the readout pixel array system: (1) silicon dioxide (SiO_2) material employed in charge-coupled devices (CCD), (2) indium tin oxide (ITO) material used in thin-film transistor (TFT) devices, and (3) indium gallium arsenide (InGaAs) applied in complementary metal-oxide-semiconductor (CMOS) devices. The variation of refractive indexes as a function of light wavelength (400–700 nm) is also provided in Figure 3 for all sensing materials [37,38]. The surface-roughness effects were examined in the range from 10 nm up to 100 nm. Three different cases were examined based on the angle of the incident light photons at the exit surface of the phosphor and the entrance surface of the sensing material: (a) $\theta = 0°$, (b) $\theta = 15°$, and (c) $\theta = 45°$.

3. Results and Discussion

The effects of surface roughness on light reflection and transmission on the intermediate surface between the CsI phosphor and the sensing materials are provided in Figures 4–6.

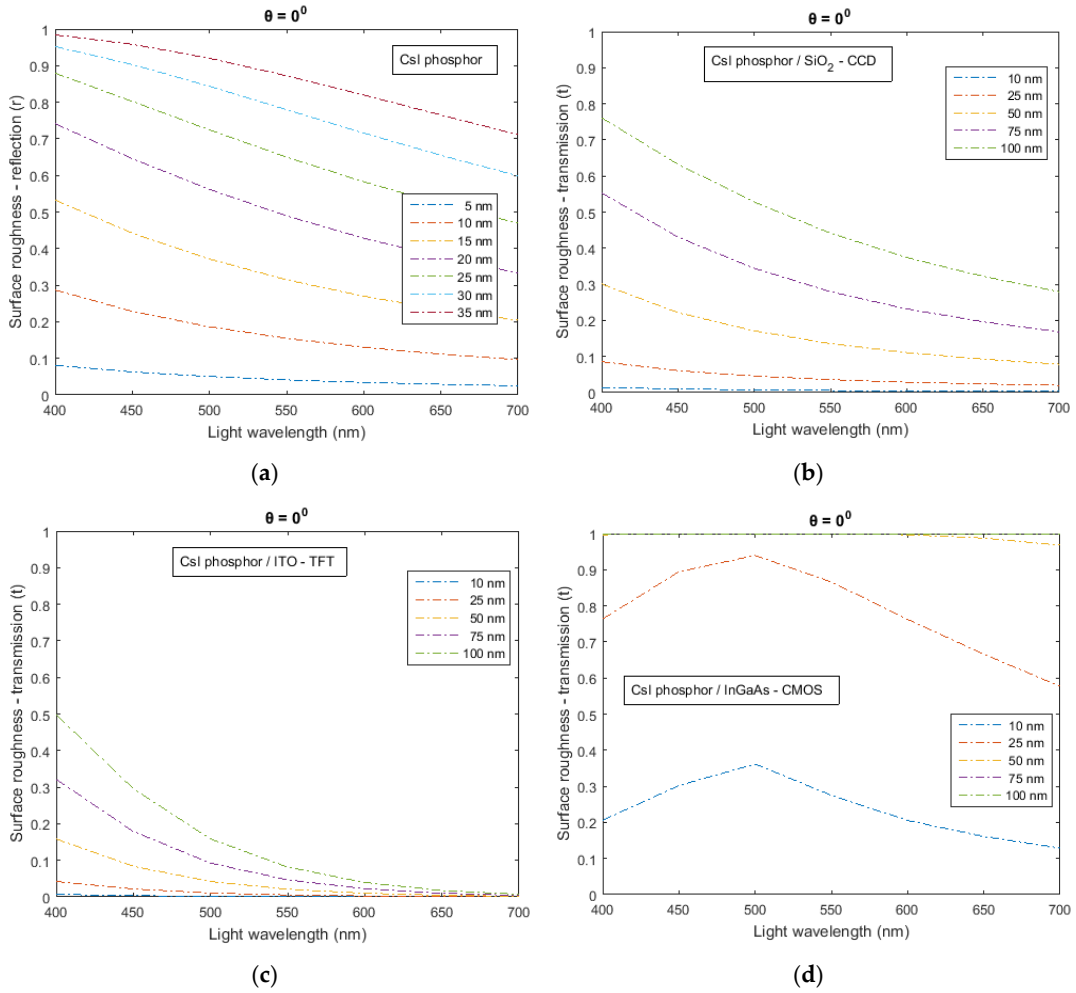

Figure 4. Figure depicts the variation of the reflection r (case **a**) and the tranmission t (cases **b**–**d**) as a function of light wavelength (400–700 nm). Figures correspond to three cases of confuguration geometries between CsI phosphor and three sensing materials: SiO_2 (employed in CCD), ITO (employed in TFT), and InGaAs (employed in CMOS), respectively. Results are provided for incident polar angle θ equal to 0°.

In particular, the results were obtained by using Equation (4) (evaluation of the reflection factor r) and Equation (5) (evaluation of the transmission factor t) and are analyzed and classified as follows. Each figure depicts four cases: (a) the first case shows the variation of the reflection factor r as a function of light wavelength (400–700 nm) for surface roughness δ values from 5 nm up to 35 nm, (b) the second case corresponds to SiO_2 sensing material and shows the variation of the transmission factor t as a function of light wavelength (400–700 nm) for surface roughness δ values from 10 *nm* up to 100 *nm*, (c) the third case corresponds to ITO sensing material and shows the variation of the transmission factor t as a function of light wavelength (400–700 nm) for surface roughness δ values from 10 nm up to 100 nm, and (d) the fourth case corresponds to InGaAs sensing material and shows the variation of the transmission factor t as a function of light wavelength (400–700 nm) for surface roughness δ values from 10 nm up to 100 nm. Results are provided in Figures 4–6 for incident polar angle θ equal to to 0°, 15°, and to 45°, respectively.

Examining and comparing the reflection factor r under similar and specific conditions, it was found to vary: (i) from 0.03 (surface roughness of 5 nm) up to 0.71 (surface roughness of 35 nm) at 700 nm light wavelength and polar angle 0°, (ii) from 0.98 (light wavelength 400 nm) down to 0.71 (light wavelength 700 nm) for surface roughness of 35 nm and polar angle 0°, and (iii) from 0.71 (polar angle 0°) down to 0.29 (polar angle 45°) at 700 nm light wavelength and surface roughness of 35 nm. As a result, the following conclusions can be drawn. The reflection factor r: (i) increases with surface-roughness value, (ii) decreases with light wavelength, and (iii) decreases with incident polar angle.

Regarding the transmission factor t, by analyzing and comparing the performance of the three sensing materials under similar conditions, general observations can be underlined.

In the case of SiO_2 sensing material: there may be observed a continuous decrease of transmission factor t from an initial value (at 400 nm) down to lower values (at 700 nm). Identically with the case of ITO sensing material, the variation of the transmission factor t is continuous, however the SiO_2 exhibits higher values under similar surface-roughness conditions. More specifically, the transmission factor t varies: (i) from 0.76 down to 0.28 for the highest value of surface roughness (100 nm). Data are provided for polar angle 0°, (ii) from 0.56 down to 0.17 for the highest value of surface roughness (100 nm). Data are provided for polar angle 15° and (iii) from 0.20 down to 0.05 (at 600 nm) for the highest value of surface roughness (100 nm). Data are provided for polar angle 45°.

In the case of ITO sensing material: there may be observed a continuous decrease of transmission factor t from an initial value (at 400 nm) down to zero value. The initial value is higher for high values of surface roughness and low values of polar angle. For example, the initial value takes: (i) the value of 0.49 for surface roughness 100 nm and 0.007 for surface roughness of 10 nm (polar angle 0°). Below 0.01 is achieved approximately around 650 nm for all cases of surface-roughness values, (ii) the value of 0.33 for surface roughness of 100 nm and 0.004 for surface roughness of 10 nm (polar angle 15°). Below 0.01 is achieved approximately around 650 nm for all cases of surface-roughness values and (iii) the value of 0.17 for surface roughness of 100 nm and 0.001 for surface roughness of 10 nm (polar angle 45°). Below 0.01 is achieved approximately around 600 nm for all cases of surface-roughness values.

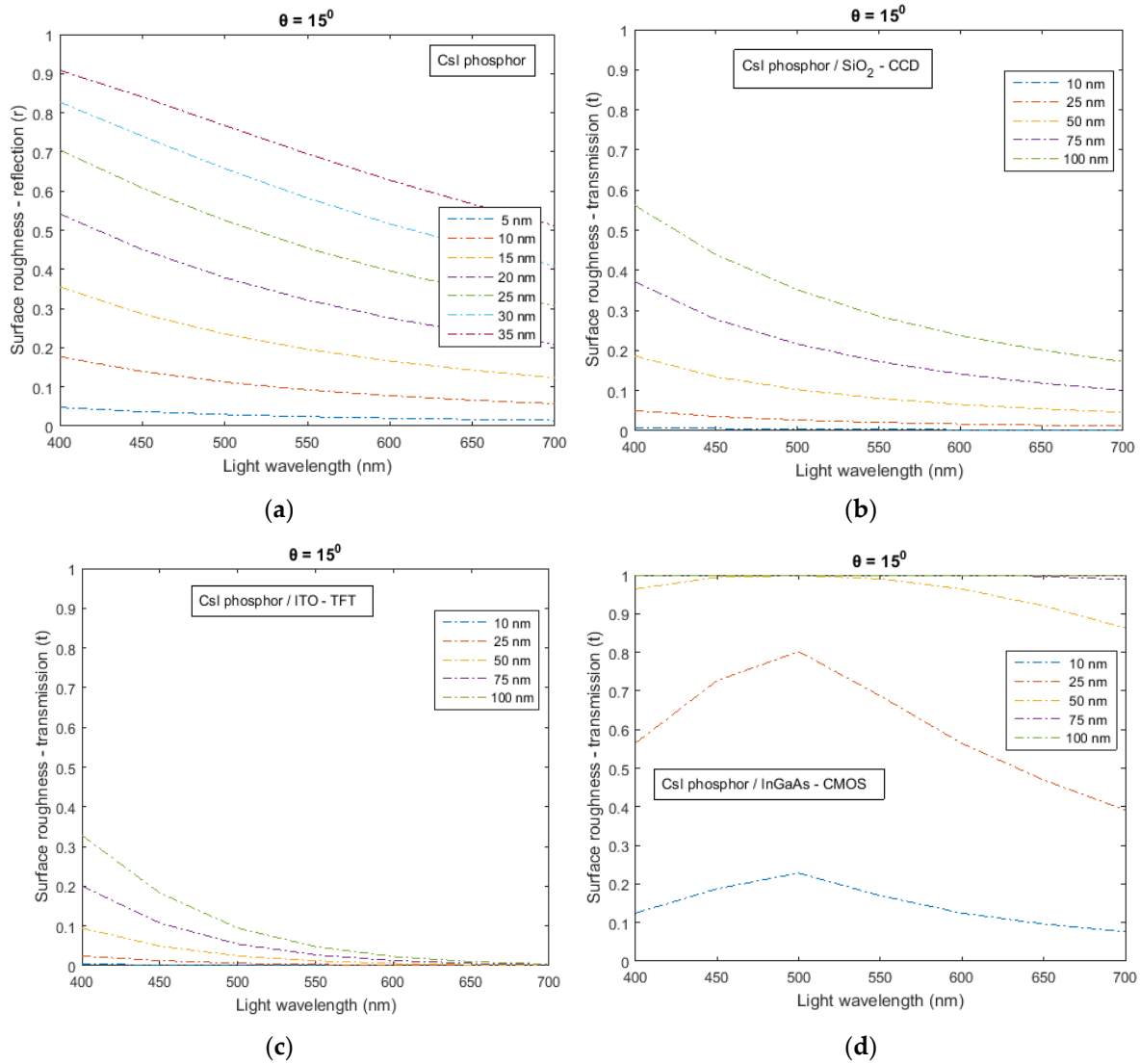

Figure 5. The figure depicts the variation of the reflection *r* (case **a**) and the tranmission *t* (cases **b**–**d**) as a function of light wavelength (400–700 nm). Figures correspond to three cases of configuration geometries between CsI phosphor and three sensing materials: SiO_2 (employed in CCD), ITO (employed in TFT), and InGaAs (employed in CMOS), respectively. Results are provided for incident polar angle θ equal to 15°.

In the case of InGaAs sensing material: there may be observed a variation of transmission factor *t* where initially there is an increase up to a maximum value and thereafter follows a decrease with light wavelength. However, this observation concerns particular surface-roughness values, which change also with the polar angle value. In particular, (i) for polar angle 0° the transmission factor *t*: (a) increases from 0.21 up to 0.36 (light wavelength 500 nm) and thereafter decreases down to 0.13, regarding the surface roughness of 10 nm, and (b) increases from 0.76 up to 0.94 (light wavelength 500 nm) and thereafter decreases down to 0.58, regarding the surface roughness of 25 nm. For higher values of surface roughness (i.e., 50 nm, 75 nm and 100 nm) the transmission factor *t* was found to be stable and almost equal to unity, (ii) for polar angle 15^0 the transmission factor *t*: (a) increases from 0.13 up to 0.23 (light wavelength 500 nm) and thereafter decreases down to 0.08, regarding the surface roughness of 10 nm, and (b) increases from 0.57 up to 0.80 (light wavelength 500 nm) and thereafter decreases down to 0.39, regarding the surface roughness of 25 nm. For higher values of surface roughness (i.e., 75 nm and 100 nm) the transmission factor *t* was found to be stable and almost equal to unity, apart from the surface value 50 nm, where a decrease occurred from unity down to

0.86 (above 550 nm up to 700 nm), and (iii) for polar angle 45° the transmission factor *t*: (a) increases from 0.06 up to 0.12 (light wavelength 500 nm) and thereafter decreases down to 0.04, regarding the surface roughness of 10 nm, (b) increases from 0.33 up to 0.54 (light wavelength 500 nm) and thereafter decreases down to 0.21, regarding the surface roughness of 25 nm, and (c) increases from 0.80 up to 0.96 (light wavelength 500 nm) and thereafter decreases down to 0.61, regarding the surface roughness of 50 nm. For higher values of surface roughness (i.e., 100 nm) the transmission factor *t* was found to be stable and almost equal to unity, apart from the surface value 75 nm, where a decrease occurred from unity down to 0.88 (above 550 nm up 700 nm).

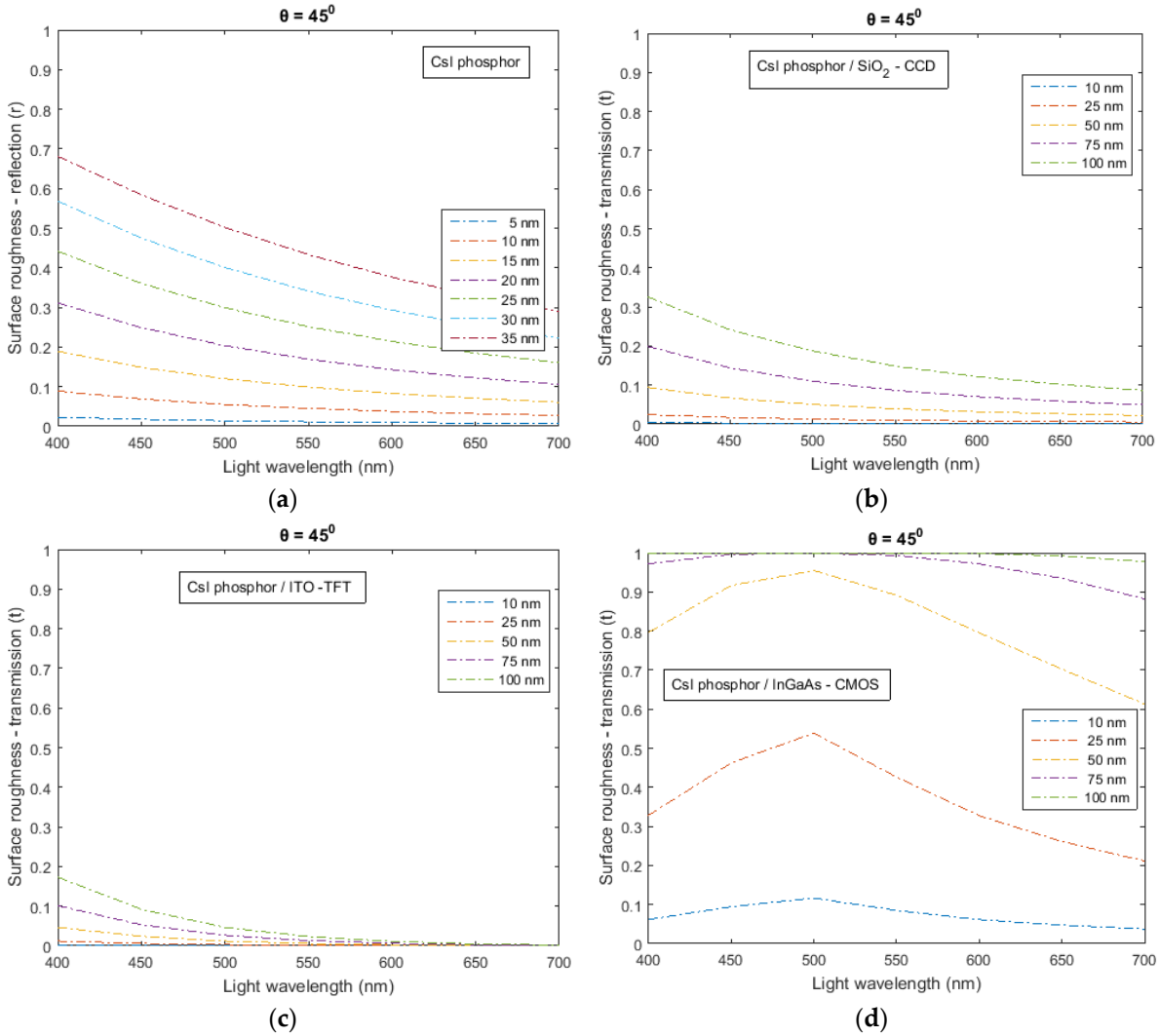

Figure 6. The figure depicts the variation of the reflection *r* (case **a**) and the tranmission *t* (cases **b**–**d**) as a function of light wavelength (400–700 nm). Figures correspond to three cases of configuration geometries between CsI phosphor and three sensing materials: SiO_2 (employed in CCD), ITO (employed in TFT), and InGaAs (employed in CMOS), respectively. Results are provided for incident polar angle θ equal to 45°.

Based on the aforementioned analysis, for the variation of transmission factor *t* the following main outcomes can be drawn: (a) for all sensing materials the variation of transmission factor *t* follows qualitatively the variation of their refractive indexes with light wavelength, as shown in Figure 3; (b)'for all sensing materials the variation of transmission factor *t* follows quantitatively the variation of: (i) surface roughness, and (ii) incident polar angle; (c) the curve of variation was found to be continuous for ITO and SiO_2 sensing materials. Between the two cases, ITO exhibited lower values and the curve

of variation was sharper than in the SiO_2 case. This section may be divided by subheadings. It should provide a concise and precise description of the experimental results, their interpretation as well as the experimental conclusions that can be drawn.

Finally, Table 1 summarizes the variation of the tranmission factor *t* with incident polar angles θ and surface roughness between CsI phosphor and the corresponding sensing materials SiO2, ITO, and InGaAs, respectively. Results are provided for light wavelength equal to 550 nm (the approximate emission peak of CsI phosphor doped with thallium activator). In particular, and for surface roughness in the range 10–100 nm, the transmission factor increases: (a) from 0.01 up to 0.44 for SiO2, from 0 up to 0.08 for ITO, and from 0.28 up to 1 for InGaAs, considering polar angle 00; (b) from 0 up to 0.29 for SiO2, from 0 up to 0.05 for ITO and from 0.17 up to 1 for InGaAs, considering polar angle 150; and (c)) from 0 up to 0.15 for SiO2, from 0 up to 0.02 for ITO and from 0.09 up to 1 for InGaAs, considering polar angle 450. Considering surface roughness of 100 nm, there was found to be a decrease of (i) 10 % for the first configuration CsI/SiO2 (angle range 00–450) and (ii) 75 % for the second configuration CsI/ITO (angle range 00–450). For the third configuration CsI/InGaAs, no variation was observed.

Table 1. The table provides the variation of the tranmission factor *t* between CsI phosphor and the corresponding sensing materials SiO_2, ITO, and InGaAs, respectively. Results are provided for incident polar angles θ equal to 0°, 15°, and 45° and surface roughness (10, 25, 50, 75, 100 nm). Data are shown for light wavelength 550 nm (the approximate emission peak of CsI phosphor doped with thallium activator).

Light Wavelength: 550 nm			
Surface Roughness (nm)	**Transmission (t)-CsI/SiO_2**		
	θ = 0°	**θ = 15°**	**θ = 45°**
10	0.01	0.00	0.00
25	0.04	0.02	0.01
50	0.14	0.08	0.04
75	0.28	0.17	0.09
100	0.44	0.29	0.15
	Transmission (t)-CsI/ITO		
	θ = 0°	**θ = 15°**	**θ = 45°**
10	0.00	0.00	0.00
25	0.01	0.00	0.00
50	0.02	0.01	0.01
75	0.05	0.03	0.01
100	0.08	0.05	0.02
	Transmission (t)-CsI/InGaAs		
	θ = 0°	**θ = 15°**	**θ = 45°**
10	0.28	0.17	0.09
25	0.87	0.69	0.43
50	1.00	0.99	0.89
75	1.00	1.00	0.99
100	1.00	1.00	1.00

4. Conclusions

Research and development in digital optical devices have become ubiquitous over the past decade with the purpose of presenting new and advanced high-performance displays for a variety of applications. Within the framework of image acquisition research, the optimization of the imaging system can be accomplished by improving the surface-roughness effects of the components embedded in the imaging chain. Regarding the surface-roughness influence between the widely used CsI phosphor material and the sensing materials (i.e., the silicon dioxide—SiO_2, the indium tin oxide—ITO, and the indium gallium arsenide—InGaAs) employed correspondingly in CCD, TFT, and CMOS image devices, the following major conclusion can be drawn: the transmission factor t of the optical signal follows qualitatively the variation of their refractive indexes and quantitatively the variation of the surface roughness and the incident polar angle.

Author Contributions: Conceptualization, P.L. and S.D.; methodology, P.L. and S.D.; software, P.L.; validation, P.L.; formal analysis, P.L.; investigation, P.L. and S.D.; writing—original draft preparation, P.L.; writing—review and editing, P.L. and S.D.; visualization, P.L.; supervision, P.L. All authors have read and agreed to the published version of the manuscript.

Funding: This research received no external funding.

Conflicts of Interest: The authors declare no conflict of interest.

References

1. Granfors, P.R.; Albagli, D. Scintillator-based flat-panel x-ray imaging detectors. *J. Soc. Inf. Disp.* **2009**, *17*, 535–542. [CrossRef]
2. Yaffe, M.J.; Rowlands, J.A. X-ray detectors for digital radiography. *Phys. Med. Biol.* **1997**, *42*, 1–39. [CrossRef] [PubMed]
3. Gruner, S.M.; Tate, M.W.; Eikenberry, E.F. Charge-coupled device area x-ray detectors. *Rev. Sci. Instrum.* **2002**, *73*, 2816–2842. [CrossRef]
4. Magnan, P. Detection of visible photons in CCD and CMOS: A comparative view. *Nucl. Instrum. Methods Phys. Res. Sect. A* **2003**, *504*, 199–212. [CrossRef]
5. Bigas, M.; Cabruja, E.; Forest, J.; Salvi, J. Review of CMOS image sensors. *Microelectron. J.* **2006**, *37*, 433–451. [CrossRef]
6. Fossum, E.R.; Ma, J.; Masoodian, S.; Anzagira, L.; Zizza, R. The quanta image sensor: Every photon counts. *Sensors* **2016**, *16*, 1260. [CrossRef] [PubMed]
7. Michail, C.; Kalyvas, N.; Valais, I.; David, S.; Seferis, I.; Toutountzis, A.; Karabotsos, A.; Liaparinos, P.; Fountos, G.; Kandarakis, I. On the response of $GdAlO_3$: Ce powder scintillators. *J. Lumin.* **2013**, *144*, 45–52. [CrossRef]
8. Kalyvas, N.; Liaparinos, P.; Michail, C.; David, S.; Fountos, G.; Wojtowicz, M.; Zych, E.; Kandarakis, I. Studying the luminescence efficiency of Lu_2O_3: Eu nanophosphor material for digital X-ray imaging applications. *Appl. Phys. A* **2012**, *106*, 131–136. [CrossRef]
9. Liaparinos, P. Examining phosphor material properties for imaging purposes: The role of the complex refractive index in the optical diffusion performance. *Biomed. Phys. Eng. Express* **2017**, *3*, 015006. [CrossRef]
10. Liaparinos, P.F. Light beam interactions and emission performance in powder phosphor materials: The role of the binder. *Nucl. Instrum. Methods Phys. Res. Sect. B* **2018**, *432*, 5–12. [CrossRef]
11. Liaparinos, P.F. LIGHTAWE—Case studies of LIGHT spread in powder materials: A montE carlo simulation tool for research and educational purposes. *Appl. Phys. B* **2019**, *125*, 151. [CrossRef]
12. Liaparinos, P.; Kalyvas, N.; Katsiotis, E.; Kandarakis, I. Investigating the particle packing of powder phosphors for imaging instrumentation technology: An examination of Gd_2O_2S: Tb phosphor. *JINST* **2016**, *11*, P10001. [CrossRef]
13. Liaparinos, P.F. Optical diffusion performance of nanophosphor-based materials for use in medical imaging. *J. Biomed. Opt.* **2012**, *17*, 126013. [CrossRef] [PubMed]
14. Liaparinos, P.; Kandarakis, I. The imaging performance of compact Lu_2O_3: Eu phosphor screens: Monte Carlo simulation for applications in mammography. *Med. Phys.* **2009**, *36*, 1985–1997. [CrossRef]

15. Schröder, S.; Duparré, A.; Coriand, L.; Tünnermann, A.; Penalver, D.H.; Harvey, J.E. Modeling of light scattering in different regimes of surface roughness. *Opt. Express* **2011**, *19*, 9820–9835. [CrossRef]
16. Zhong, N.; Zhu, X.; Liao, Q.; Wang, Y.; Chen, R.; Sun, Y. Effects of surface roughness on optical properties and sensitivity of fiber-optic evanescent wave sensors. *Appl. Opt.* **2013**, *52*, 3937–3945. [CrossRef]
17. Alves, H.P.; Nascimento, J.F.; Fontana, E.; Coêlho, I.J.S.; Martins Filho, J.F. Transition Layer and Surface Roughness Effects on the Response of Metal-based Fiber-optic Corrosion Sensors. *J. Light. Technol.* **2018**, *36*, 2597–2605. [CrossRef]
18. Sequeira, F.; Cennamo, N.; Rudnitskaya, A.; Nogueira, R.; Zeni, L.; Bilro, L. D-Shaped POF Sensors for Refractive Index Sensing—The Importance of Surface Roughness. *Sensors* **2019**, *19*, 2476. [CrossRef]
19. Agarwal, S.; Giri, P.; Prajapati, Y.K.; Chakrabarti, P. Effect of Surface Roughness on the Performance of Optical SPR Sensor for Sucrose Detection: Fabrication, Characterization, and Simulation Study. *IEEE Sens. J.* **2016**, *16*, 8865–8873. [CrossRef]
20. Cahill, B. Laser-Based Fibre-Optic Sensor for Measurement of Surface Properties. Master's Thesis, Dublin City University, Dublin, Ireland, 1998.
21. Le Bosse, J.C.; Hansali, G.; Lopez, J.; Dumas, J.C. Characterisation of surface roughness by laser light scattering: Diffusely scattered intensity measurement. *Wear* **1999**, *224*, 236–244. [CrossRef]
22. Cahill, B.; El Baradie, M.A. LED-based fibre-optic sensor for measurement of surface roughness. *J. Mater. Process. Technol.* **2001**, *119*, 299–306. [CrossRef]
23. Liu, J.; Yamazaki, K.; Zhou, Y.; Matsumiya, S. A reflective fiber optic sensor for surface roughness in-process measurement. *JMST* **2002**, *124*, 515–522. [CrossRef]
24. Feidenhans, N.A.; Hansen, P.E.; Pilný, L.; Madsen, M.H.; Bissacco, G.; Petersen, J.C.; Taboryski, R. Comparison of optical methods for surface roughness characterization. *Meas. Sci. Technol.* **2015**, *26*, 085208. [CrossRef]
25. Mitsui, K. In-process sensors for surface roughness and their applications. *Precis. Eng.* **1986**, *8*, 212–220. [CrossRef]
26. Bohren, C.F.; Huffman, D.R. *Absorption and Scattering of Light by Small Particles*; Wiley: New York, NY, USA, 1983.
27. Born, M.; Wolf, E. *Principles of Optics: Electromagnetic Theory of Propagation, Interference and Diffraction of Light*, 6th ed.; Pergamon Press: Oxford, UK, 1986.
28. Hecht, E. *Optics*, 2nd ed.; Addison-Wesley Publishing Company, Inc.: Boston, MA, USA, 1987.
29. Badano, A.; Sempau, J. MANTIS: Combined x-ray, electron and optical Monte Carlo simulations of indirect radiation imaging systems. *Phys. Med. Biol.* **2006**, *51*, 1545–1561. [CrossRef] [PubMed]
30. Roos, A.; Ronnow, D. Diffuse reflectance and transmittance spectra of an interference layer: 1. Model formulation and properties. *Appl. Opt.* **1994**, *33*, 7908–7917. [CrossRef]
31. Bhushan, B. Chapter 2 Surface Roughness Analysis and Measurement Techniques. In *Modern Tribology Handbook*, 1st ed.; Taylor & Francis Group: Boca Raton, FL, USA, 2000.
32. Peiponen, K.-E.; Tsuboi, T. Metal surface roughness and optical reflectance. *Opt. Laser Technol.* **1990**, *22*, 127–130. [CrossRef]
33. Bennett, H.E.; Porteus, J.O. Relation between surface roughness and specular reflectance at normal incidence. *JOSA* **1961**, *51*, 123–129. [CrossRef]
34. Kim, H.K.; Cunningham, I.A.; Yin, Z.; Cho, G. On the Development of Digital Radiography Detectors: A Review. *Int. J. Precis. Eng. Manuf.* **2006**, *9*, 86–100.
35. Polyanskiy, M.N. Refractive Index Database. Available online: https://refractiveindex.info/ (accessed on 3 February 2020).
36. Peixoto, A.C.; Silva, A.F. Smart devices: Micro-and nanosensors. *Bioinspired Mater. Med. Appl.* **2017**, 297–329. [CrossRef]
37. Filmetrics KLA Company. Available online: https://www.filmetrics.com/refractive-index-database (accessed on 3 February 2020).
38. Dinges, H.W.; Burkhard, H.; Lösch, R.; Nickel, H.; Schlapp, W. Refractive indices of InAlAs and InGaAs/InP from 250 to 1900 nm determined by spectroscopic ellipsometry. *Appl. Surf. Sci.* **1992**, *54*, 477–481. [CrossRef]